AIAA JOURNAL
Vol. 48, No. 2, February 2010

Theoretical Modeling of Two-Body Interaction in Supersonic Flow

Alexander V. Fedorov* and Vitaly G. Soudakov†
Moscow Institute of Physics and Technology, 140180 Zhukovsky, Russia
and
Norman D. Malmuth‡
Teledyne Scientific and Imaging, Thousand Oaks, California 91360

DOI: 10.2514/1.40592

Atmospheric and space launch stage separation depends on the aerodynamic interference between separating bodies. Quick means of estimating and controlling repulsion or attraction lift associated with this interaction are an important enabling technology to achieve the best compromise between launch separation rocket motor weight and safe staging. Asymptotic methods, scattering, and slender-body theories are used to obtain systematic approximation schemes that advantageously couple with computational methods. Theoretical solutions for the lift interference between two bodies in supersonic flow agree well with numerical solutions. The theory sheds light on important scattering phenomena not previously recognized as relevant to this problem. The analysis helps to identify lumped dimensionless parameters and provides scaling laws as well as closed-form expressions for the interference not accessible solely from computations. These results can be used for interpolation and extrapolation of computational fluid dynamics solutions as well as efficient testing and design of flight vehicles.

Nomenclature

A	=	cross-sectional body area
a	=	body radius
C_L	=	integral lift coefficient
c_L	=	local lift coefficient
h	=	vertical distance between bodies' axes
L	=	lift force
l	=	body length
l_n	=	body nose length
M	=	Mach number
p	=	pressure
T	=	temperature
u, v, w	=	velocity components
x, y, z	=	Cartesian coordinates
x_0	=	streamwise distance from the nose tip to the point where shock crosses the body axis
α	=	induced angle of attack
ε	=	characteristic flow deflection
ρ	=	density
ϕ	=	perturbation potential

I. Introduction

MULTIBODY aerodynamics and flow control are critically important aspects of high-speed flight vehicles. The latter includes transatmospheric vehicle concepts that will skip outside and inside the Earth's atmospheric layers to obtain global cross-range capability. Besides lift-to-drag ratio, the fuel-weight fraction is a metric that needs to be optimized to meet this requirement. In launch applications, overly conservative sizing of stage separation rocket motors adversely influences this weight fraction and reduces payload. The correctness of tradeoff decisions that deal with these factors depends on our understanding of the fluid dynamics relevant to the multibody interaction. Although this problem has received much attention as exemplified by [1–4], more effort is needed to understand the underlying basic physics and essential parameters.

Experimental studies [5–8] do not cover all cases of this multiparametric problem. They, however, provide useful data sets for verification of theoretical, semiempirical, and computational tools. Computational fluid dynamics (CFD) has been the main approach for the aerospace engineer and designer in obtaining aerodynamic characteristics of multibody configurations [9–12]. Yet, despite the power of CFD, challenges still exist to predict drag, lift, and other quantities rapidly enough for conceptual design. Typical CFD calculations require significant amounts of preprocessing, a large portion of which involves grid generation. Conceptual design optimization also requires the study of hundreds to thousands of parametric variations as well as the interplay of physical intuition and compromises based on aerodynamic reasoning and systems' impacts. In this connection, it is reasonable to apply a combined asymptotic and numerical approach, which simplifies the problem, reduces the dimensionality of the independent variable and parameter space, and provides insight for the gridding and zonal decompositions [13]. Furthermore, theory can facilitate interpolation between computational solutions.

The general mathematical ideas and key unit problems associated with aerodynamics of two bodies interacting in a supersonic flow were discussed in [14]. The linear supersonic slender-body theory provides a coherent picture of the wave train occurring between two bodies of revolution. Significant interference pressure and drag were obtained to dominant order whereas lift and pitching moment were of higher order. Nevertheless, the latter are of critical importance for predicting of the body separation process.

The lift and pitching moment are associated with local scattering of shock waves induced by interacting bodies. Detailed theoretical analysis of multiple shock-wave scatterings for the wedge–slender-body configuration was conducted in [15]. The problem was analyzed using the slender-body theory with the ratio of the body radius to the separation distance being treated as a small parameter. The linear form of Prandtl–Glauert equation for the perturbation velocity potential was used for modeling of the disturbance flowfield. An initial boundary value problem for the impingement of a

Presented as Paper 4341 at the 5th AIAA Theoretical Fluid Mechanics Conference, Seattle, WA, 23–26 June 2008; received 26 August 2008; revision received 5 March 2009; accepted for publication 26 April 2009.

*Associate Professor, Department of Aeromechanics and Flight Engineering; fedorov@falt.ru. Member AIAA.
†Associate Professor, Department of Aeromechanics and Flight Engineering; vit_soudakov@mail.ru. Member AIAA.
‡Principal Scientist. Fellow AIAA.

wedge-induced shock on a cylindrical body surface was solved using transform calculus. The shock wave was expressed as a sum of elementary waves that are similar to plane acoustic waves interacting with the cylinder surface. This similarity helped to use methods of scattering theory and obtain an analytical solution providing distributions of the local lift coefficient along the cylinder axis as well as the total lift coefficient. The theoretical results agree well with corresponding numerical solutions of three-dimensional Euler equations and with experiment [6]. For example, the difference between the experimental lift distribution (measured on the blunt-base parabolic body of revolution in the flowfield induced by a circular-arc wing in the Mach = 2 freestream) and the theoretical one is less than 10%, despite the fact that the body radius varies in the interaction region and the wing thickness is not very small [15].

In this paper, the interference between two bodies of revolution is treated with emphasis on the lift force. The cross-sectional shape of both bodies is a function of the axial coordinate, that is, each of the bodies generates flow disturbances with appreciable streamwise variations over the body length. The problem is analyzed using two essentially different approaches. The first is based on the shock wave scattering theory and provides a local solution, which is an extension of the theoretical model [15] to the case of two-body interaction (Sec. II). The second uses asymptotic methods and the basic idea of slender-body theory: replace bodies by distributions of sources and doublets (Sec. III). These two approaches supplement each other: the first clarifies flow details in local regions associated with rapid changes of the incoming (parent-body-induced) flowfield near the parasite body whereas the second provides a global structure of the lift distribution. The lift coefficients resulted from the local and global solutions are compared with the Euler CFD prediction. In Sec. IV, the global solution is applied to the body–wedge interaction.

II. Lift Due to Two-Body Interaction Predicted by Local Analysis

Consider a two-body configuration in a supersonic freestream (Fig. 1). Each of the bodies has the length l^* and a sharp nose that is smoothly matched with a cylindrical afterbody of radius a^*. Hereinafter, asterisks denote dimensional quantities. It is assumed that the body nose length is $l_n^* = O(l^*)$ and the body thickness ratio is small, $\varepsilon = a^*/l^* \ll 1$. The distance h^* between bodies is assumed to be large compared with the afterbody radius a^*. The nondimensional coordinates are $(x, y, z) = (x^*, y^*, z^*)/l^*$. The flow velocity and density are made dimensionless using their freestream quantities U_∞^* and ρ_∞^*, the pressure is normalized by $\rho_\infty^* U_\infty^{*2}$.

The first (parent) body generates a conical disturbance that is scattered by the second (parasite) body surface. Our objective is to predict the local c_L and integral C_L lift coefficients defined as

$$c_L(x^*) \equiv \frac{2l^*}{\rho_\infty^* U_\infty^{*2} \pi a^{*2}} \frac{\mathrm{d}L^*}{\mathrm{d}x^*}$$

$$C_L(x^*) \equiv \frac{2L^*(x^*)}{\rho_\infty^* U_\infty^{*2} \pi a^{*2}} = \frac{1}{l^*} \int_0^{x^*} c_L(x^*)\mathrm{d}x^* \tag{1}$$

where L^* is the lift force directed along the y axis.

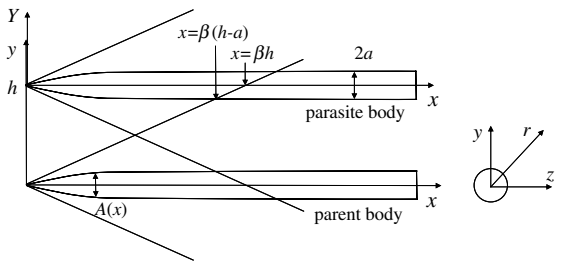

Fig. 1 Schematics of the two-body configuration.

A. Theoretical Analysis

The parent body of cross-sectional area $A(x)$ induces the flow potential [16,17]

$$\phi = -\frac{1}{2\pi} \int_0^x \frac{H(x-\beta r-\xi)A'(\xi)\mathrm{d}\xi}{\sqrt{(x-\xi)^2-\beta^2 r^2}} \tag{2}$$

where $r = \sqrt{y^2+z^2}$ is radial coordinate, $\beta = \sqrt{M_\infty^2 - 1}$, and $H(x)$ is Heaviside function. The Laplace transform vs x

$$L_p[\phi] \equiv \bar{\phi}(p, y, z) \equiv \int_0^\infty \phi e^{-px}\mathrm{d}x \tag{3}$$

gives

$$\bar{\phi} = -S(p) L_p\left[\frac{H(x-\beta r)}{\sqrt{x^2-\beta^2 r^2}}\right], \qquad S(p) = L_p\left[\frac{1}{2\pi}A'(x)\right] \tag{4}$$

Because the function $H(x-\beta r)/\sqrt{x^2-\beta^2 r^2}$ has the Laplace transform $K_0(\beta p r)$, where K_0 is a modified Bessel function [18], Eq. (4) can be written in the form

$$\bar{\phi} = -S(p) K_0(\beta r p) \tag{5}$$

The inverse Laplace transform of Eq. (5) gives

$$\phi = L_p^{-1}[\bar{\phi}] = \frac{1}{2\pi i} \int_{c+i_\infty}^{c+i_\infty} [-S(p) K_0(\beta r p)] e^{px}\mathrm{d}p \tag{6}$$

The parent-body induced disturbances radiate a cylindrical part of the parasite body as schematically shown in Fig. 1. In accord with Eq. (6), the parasite body feels disturbances with the Laplace components in Eq. (5) at $r = h + Y$, where Y is measured from the parasite-body axis. In the case of $h \gg a$, the argument $s = \beta p r$ is large and the modified Bessel function $K_0(s)$ is approximated by the asymptotic expansion [14]

$$K_0(s) = \sqrt{\frac{\pi}{2s}} e^{-s}[1 + O(s^{-1})] \tag{7}$$

Then, Eq. (5) is expressed as

$$\bar{\phi}(p, y, z) e^{px} = -S(p) \sqrt{\frac{\pi}{2p\beta h}} e^{p(x-\beta h-\beta Y)}[1 + O((p\beta h)^{-1})]$$

$$r = h + Y \tag{8}$$

With the substitution of variables $p = i\alpha$ and $k = \beta\alpha$, Eq. (8) is expressed in the plane wave form

$$\bar{\phi}(p, y, z) e^{px} = B(\alpha, h) e^{i\alpha x - ikY}[1 + O((kh)^{-1})] \tag{9}$$

$$B(\alpha, h) = -S(i\alpha) \sqrt{\frac{\pi}{2ikh}} e^{-ikh} \tag{10}$$

Equation (9) indicates that the parasite body scatters incoming plane waves of amplitudes in Eq. (10). As shown in [15], the local lift coefficient induced by a plane wave of amplitude $B = 1$ is

$$\bar{c}_L(\alpha) = -\frac{8i\alpha}{\pi k a^2 H_1^{(2)\prime}(ka)} \tag{11}$$

where $H_1^{(2)}$ is Hankel functions of the second kind [18]. Multiplying Eq. (11) by the amplitude in Eq. (10) and integrating over the entire spectrum of incoming waves one can obtain

$$c_L(x; h, a, \beta) = \frac{1}{2\pi} \int_{-\infty-ic}^{+\infty-ic} S(i\alpha) \sqrt{\frac{\pi}{2ikh}} \frac{8i\alpha}{\pi k a^2 H_1^{(2)\prime}(ka)} e^{i\alpha x - ikh}\mathrm{d}\alpha \tag{12}$$

With the new variables $\tilde{k} = \beta a \alpha$ and $\tilde{x} = [x - \beta(h-a)]/(\beta a)$, where $\tilde{x} = 0$ corresponds to the point at which the leading-edge

shock crosses the parasite-body surface (Fig. 1), the local lift coefficient in Eq. (12) is expressed as

$$c_L(\tilde{x};h,a,\beta) = \frac{8}{\pi\beta^2 a^3}\sqrt{\frac{\pi a}{2h}}\left[\frac{1}{2\pi}\int_{-\infty-ic}^{+\infty-ic}\sqrt{\frac{1}{i\tilde{k}}}\frac{S(i\tilde{k}/\beta a)}{H_1^{(2)\prime}(\tilde{k})}ie^{-i\tilde{k}}e^{i\tilde{k}\tilde{x}}\mathrm{d}\tilde{k}\right] \quad (13)$$

With the substitution $\tilde{k} = -i\tilde{p}$ this relation is written as the inverse Laplace transform

$$c_L(\tilde{x};h,a,\beta) = \frac{8}{\pi\beta^2 a^3}\sqrt{\frac{\pi a}{2h}}L_{\tilde{p}}^{-1}\left[\frac{iS(\tilde{p}/\beta a)}{\tilde{p}^{1/2}H_1^{(2)\prime}(-i\tilde{p})}e^{-\tilde{p}}\right] \quad (14)$$

Integration of Eq. (14) over the parasite-body length leads to the integral lift coefficient

$$C_L = \int c_L(x)\mathrm{d}x = \frac{8}{\pi a^2\beta}\sqrt{\frac{\pi a}{2h}}L_{\tilde{p}}^{-1}\left[\frac{iS(\tilde{p}/\beta a)}{\tilde{p}^{3/2}H_1^{(2)\prime}(-i\tilde{p})}e^{-\tilde{p}}\right] \quad (15)$$

B. Cylindrical Body with a Sharp Nose

As an example, consider the parent body comprising a cylindrical afterbody and a sharp nose of the shape shown in Fig. 2

$$r_b(x) = a\sin\left(\frac{\pi}{2}\frac{x}{l_n}\right), \qquad 0 < x < l_n \quad (16)$$

The parasite body has the same radius a of its cylindrical part. Substitution of the nose cross-sectional area $A(x) = \pi r_b^2(x)$ into Eq. (4) gives

$$S(\tilde{p}/\beta a) = \frac{a^2}{2}\left[\frac{1}{2}(\pi\beta a/l_n)^2\frac{1+e^{-\tilde{p}l_n/\beta a}}{\tilde{p}^2+(\pi\beta a/l_n)^2}\right] \quad (17)$$

Using the normalized nose length $\bar{l}_n = l_n/(\beta a)$, Eq. (17) is expressed in the form

$$S(\tilde{p}/\beta a) = \frac{a^2}{2}Q(\tilde{p},\bar{l}_n), \qquad Q(\tilde{p},\bar{l}_n) = \frac{1}{2}(\pi/\bar{l}_n)^2\frac{1+e^{-\tilde{p}\bar{l}_n}}{\tilde{p}^2+(\pi/\bar{l}_n)^2} \quad (18)$$

Substitution of Eq. (18) into Eqs. (14) and (15) leads to the local lift coefficient

$$c_L(\tilde{x};h,\beta,a,\bar{l}_n) = \sqrt{\frac{\pi a}{2h}}\frac{4}{\pi\beta^2 a}G_0(\tilde{x},\bar{l}_n)$$
$$G_0(\tilde{x},\bar{l}_n) = L_{\tilde{p}}^{-1}\left[\frac{iQ(\tilde{p},\bar{l}_n)}{\tilde{p}^{1/2}H_1^{(2)\prime}(-i\tilde{p})}e^{-\tilde{p}}\right] \quad (19)$$

and the integral lift coefficient

$$C_L(\tilde{x},h,\beta,a,\bar{l}_n) = \frac{4}{\pi\beta}\sqrt{\frac{\pi a}{2h}}I_0(\tilde{x},\bar{l}_n)$$
$$I_0(\tilde{x},\bar{l}_n) = L_{\tilde{p}}^{-1}\left[\frac{iQ(\tilde{p},\bar{l}_n)}{\tilde{p}^{3/2}H_1^{(2)\prime}(-i\tilde{p})}e^{-\tilde{p}}\right] \quad (20)$$

The functions $G_0(\tilde{x},\bar{l}_n)$ and $I_0(\tilde{x},\bar{l}_n)$ can be calculated once and for all. They are shown in Figs. 3–6 for $\bar{l}_n = 2$, 4, 6, and 8, respectively.

The integral lift coefficient $C_L(\tilde{x}) \to 0$ as $\tilde{x} \to \infty$. This is confirmed by considering Eq. (20) for small $\tilde{p}$

$$Q(\tilde{p},\bar{l}_n) \to \frac{1}{2}(\pi/\bar{l}_n)^2, \qquad H_1^{(2)\prime}(-i\tilde{p}) \to =i\frac{2}{\pi\tilde{p}^2}, \qquad \tilde{p} \to 0 \quad (21)$$

that gives

$$I_0(\tilde{x},\bar{l}_n) = \frac{\pi}{4}(\pi/\bar{l}_n)^2 L_{\tilde{p}}^{-1}\left[\frac{1}{\tilde{p}^{1/2}}e^{-\tilde{p}}\right]$$
$$= \frac{\pi}{4}(\pi/\bar{l}_n)^2\frac{1}{\sqrt{\pi(\tilde{x}-1)}} \to 0 \quad \text{as } \tilde{x} \to \infty \quad (22)$$

Thus, the total lift induced by the first scattering is zero. As shown in [15], the second and higher scatterings also give zero contributions in the total lift. However, this limit is achieved for quite large $\tilde{x}$. For the nose length $\bar{l}_n = 2$ ($l_n^* = 2\beta a^*$) the function $I_0(\tilde{x},\bar{l}_n)$ vanishes for $\tilde{x} > 10$ corresponding to $x^* - \beta h^* > 9\beta a^*$ (Fig. 3). For all cases shown in Figs. 3–6, the lift force is cumulated over a length larger than $2l_n^*$. This indicates that the lift due to scattering is distributed rather than local. It can be treated as local (in units of the body length l^*) in the case of $l_n^* \ll l^*$ that seems to be of low practical interest. To emphasize this feature we will consider in the next section the parent body of a sharp cone shape.

C. Sharp Cone

If the parent body is a sharp cone of cross-sectional area $A(x) = \varepsilon^2\pi x^2$, then $S(p) = \varepsilon^2/p^2$. In this case, the local and integral lift coefficients are expressed as

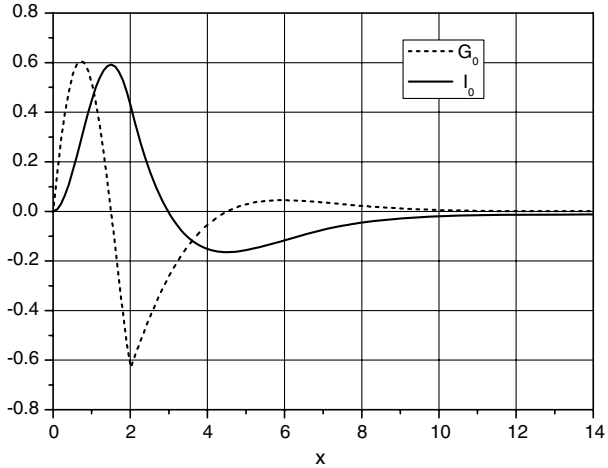

Fig. 3 Functions $G_0(\tilde{x},\bar{l}_n)$ and $I_0(\tilde{x},\bar{l}_n)$ for $\bar{l}_n = 2$.

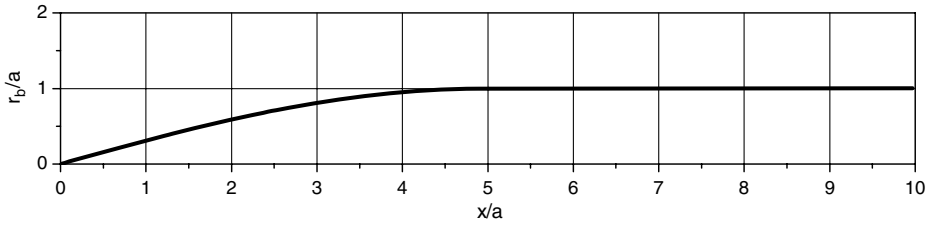

Fig. 2 Parent-body radius r_b/a as a function of x/a, nose length $l_n = 5a$.

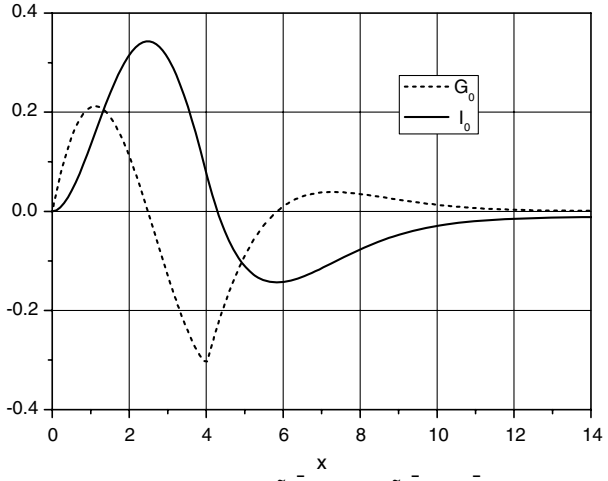

Fig. 4 Functions $G_0(\tilde{x}, \bar{l}_n)$ and $I_0(\tilde{x}, \bar{l}_n)$ for $\bar{l}_n = 4$.

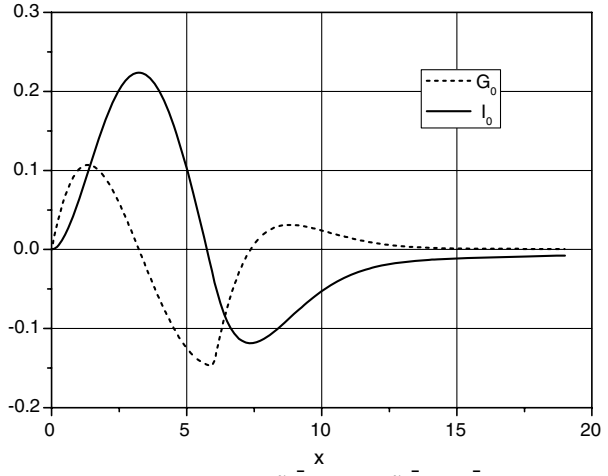

Fig. 5 Functions $G_0(\tilde{x}, \bar{l}_n)$ and $I_0(\tilde{x}, \bar{l}_n)$ for $\bar{l}_n = 6$.

$$c_L(\tilde{x}; h, a, \beta) = \varepsilon^2 \sqrt{\frac{\pi a}{2h}} \frac{8}{\pi a} G_0(\tilde{x})$$

$$G_0(\tilde{x}) = L_{\tilde{p}}^{-1}\left[\frac{i}{\tilde{p}^2 \tilde{p}^{1/2} H_1^{(2)\prime}(-i\tilde{p})} e^{-\tilde{p}}\right] \tag{23}$$

$$C_L = \varepsilon^2 \frac{8\beta}{\pi} \sqrt{\frac{\pi a}{2h}} I_0(\tilde{x}), \qquad I_0(\tilde{x}) = L_{\tilde{p}}^{-1}\left[\frac{i}{\tilde{p}^2 \tilde{p}^{3/2} H_1^{(2)\prime}(-i\tilde{p})} e^{-\tilde{p}}\right] \tag{24}$$

Using expansion of $\bar{I}_0(\tilde{p})$ for small $\tilde{p}$ and taking the inverse Laplace transform, we obtain an asymptotic behavior of $I_0(\tilde{x})$

$$I_0(\tilde{x}) = L_{\tilde{p}}^{-1}\left[\frac{\pi}{2} \frac{e^{-\tilde{p}}}{\tilde{p}^{3/2}}\right] = \sqrt{\pi(\tilde{x} - 1)}, \qquad \tilde{x} \to \infty \tag{25}$$

The functions $G_0(\tilde{x})$ and $I_0(\tilde{x})$ are shown in Figs. 7 and 8. The function $I_0(\tilde{x})$ quickly tends to its asymptotic form in Eq. (25). The lift force induced by a sharp cone grows monotonically with $\tilde{x}$. This is contrasted to the wedge–cylinder interaction [15] for which the lift force tends to a finite value as $\tilde{x} \to \infty$ (it is cumulated over a finite length $\sim 5a$).

D. Comparison with Euler CFD Solutions

To estimate accuracy of the leading-order asymptotic solution, CFD modeling of the two-body interaction has been performed using three-dimensional Euler equations. Numerical solutions were obtained using an implicit finite-volume method. The governing equations are approximated by a conservative scheme. The flux vector is evaluated by an upwind flux-difference splitting [19]. The MUSCL algorithm is applied with the third-order total variation diminishing space discretization [20]. The time marching is proceeded until a steady-state solution sets in. The computational

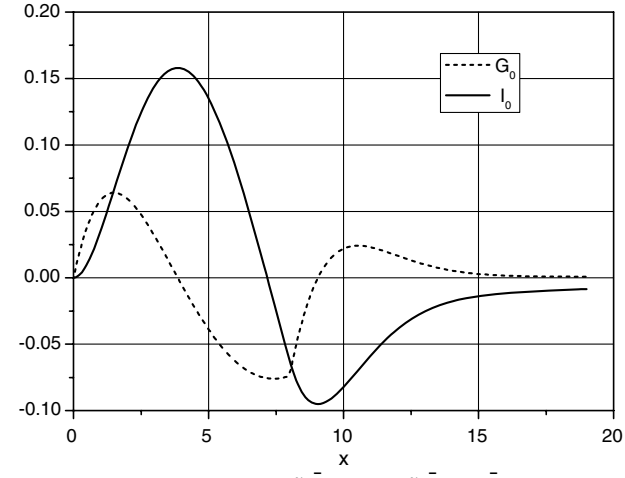

Fig. 6 Functions $G_0(\tilde{x}, \bar{l}_n)$ and $I_0(\tilde{x}, \bar{l}_n)$ for $\bar{l}_n = 8$.

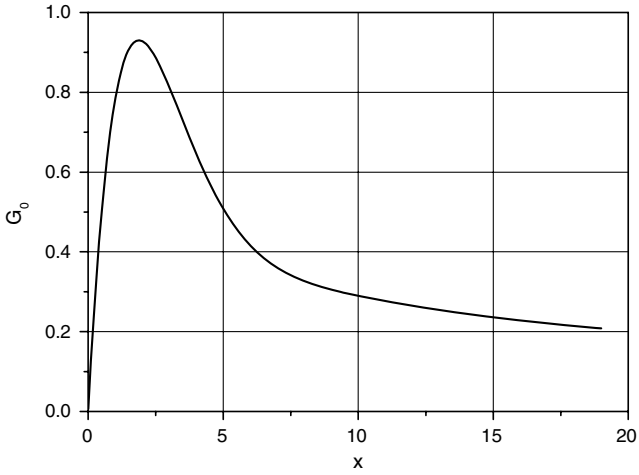

Fig. 7 Function $G_0(\tilde{x})$.

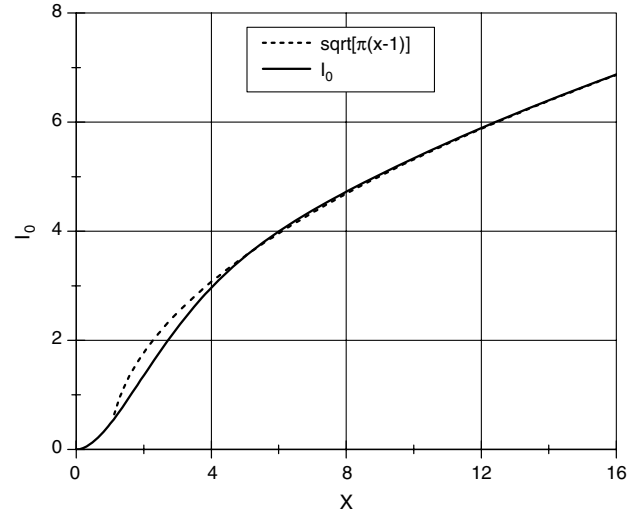

Fig. 8 Function $I_0(\tilde{x})$.

grid had a cylindrical configuration with 180 cells in the x direction, 120 cells in the radial direction, and 110 cells in the azimuth direction (the total number of grid nodes is approximately 2.3×10^6). Computations with finer grids (each of them had a doubled number of nodes in one of three dimensions) showed that the difference between solutions is less than 1.5% for typical cases discussed hereafter.

Calculations were carried out for the freestream Mach number $M_\infty = 2$ and specific heat ratio $\gamma = 1.4$. The interacting bodies have identical shapes. The vertical distance between their axes is $h = 16a$. This configuration is equivalent to a single body located over a reflection plane at a distance $h/2$ (Fig. 9). The body nose of length $l_n = 18a$ has the shape $r_b = a\sin(\pi x/2l_n)$, $0 \le x \le l_n$. Near the nose tip $x \to 0$ the apex half-angle is $\alpha \approx 5$ deg.

Figure 9 shows the computational domain. Conditions on the inflow boundary correspond to the unperturbed freestream. On the top and right-side boundaries, nonreflection conditions are imposed to minimize effects of these boundaries on numerical solutions. On the left-side and bottom boundaries, the flow symmetry conditions are used. On the outflow, the linear extrapolation condition is imposed. The distance from the bottom boundary to the body axis is $h/2 = 8a$, the distance from the body axis to the top boundary is $H_y = 35a$, and the distance from the body axis to the right boundary is $H_z = 35a$. The longitudinal length of the computational domain is $L_x = 45a$. With these parameters the computational domain includes the first-scattering region that is located downstream from the point $x_0 \approx (h-a)\sqrt{M^2-1} \approx 26a$ and has the characteristic length $\Delta \approx 10\beta a \approx 17a$.

The static pressure contours in the symmetry plane (Fig. 10) indicate that the body nose induces a conical bow shock. Behind this shock a high-pressure region is followed by a low-pressure region. Reflection from the bottom boundary gives another set of pressure disturbances. They propagate toward the body and interact with its cylindrical surface. The CFD data were processed to obtain the lift distribution associated with this interaction. The theory predicts the initial point $x_0 = \beta(h-a) \approx 26a$, at which the parent-body-induced shock wave crosses the parasite-body surface, although the CFD solution gives $x_0 \approx 25a$. To compare the lift distributions, the theoretical initial point was shifted to the CFD initial point. As shown in Fig. 11 the theoretical distribution of $c_L(x)$ given by Eq. (19) (solid line) mimics the CFD distribution (symbols). The 18% discrepancy between theory and numerical data can be reduced by considering higher-order terms of the asymptotic approximation.

Note that the asymptotic solution of scattering problem provides the local and integral lift coefficients in compact analytical forms. This tremendously simplifies predictions of the lift during the separation process. A combination of these results with the wave-train solutions [14] providing the wave drag can be used for quick estimates of aerodynamic loads on interacting bodies with low computational cost.

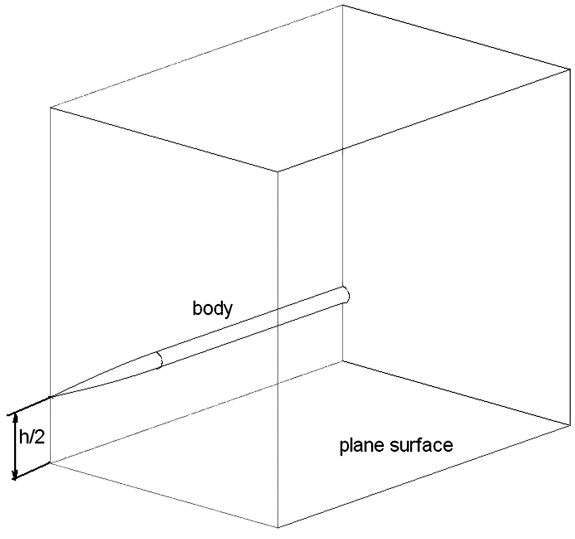

Fig. 9 Computational domain.

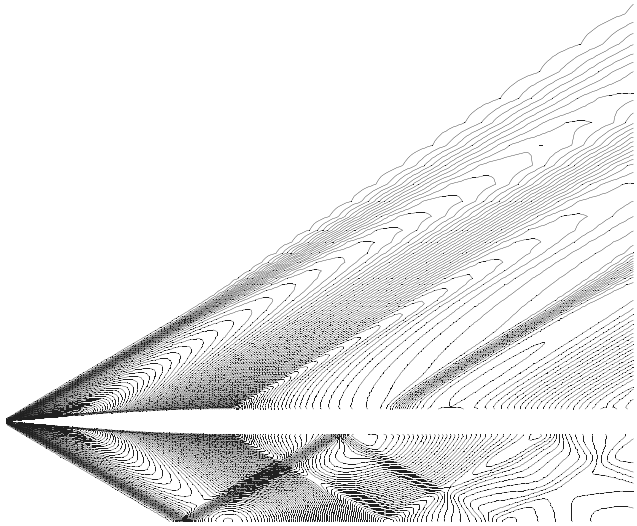

Fig. 10 Static pressure field in the symmetry plane.

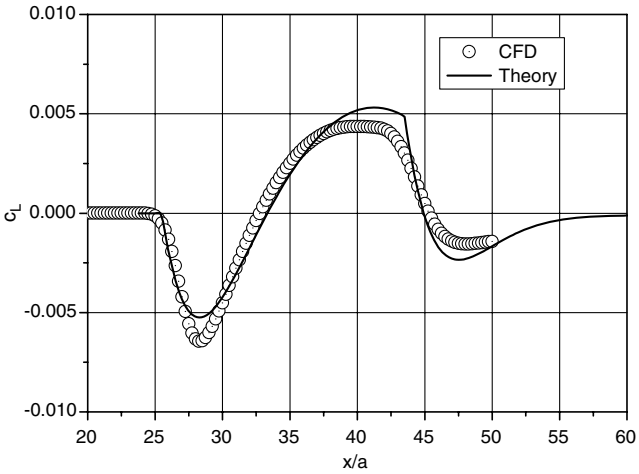

Fig. 11 Comparison of the theoretical distribution of $c_L(x)$ (solid line) with the Euler CFD solution (symbols); $M_\infty = 2$, $h = 16a$, $l_n = 18a$.

III. Lift Due to Two-Body Interaction Predicted by Global Analysis

A. Theoretical Analysis

If the parent body is a two-dimensional wing or it is a body of revolution located at a vertical distance $h^* \sim l^*$ from the parasite body, then the latter is radiated by approximately (with accuracy $O(\varepsilon^2)$) two-dimensional disturbances. In this case, it is feasible to conduct an asymptotic analysis of the global problem associated with the streamwise length scale $\sim l^*$ (notations are shown in Fig. 12). The flow potential $\phi = \phi^*/(U_\infty^* l^*)$ is expressed as a superposition of the freestream potential, the parent-body-induced potential φ_1, and the parasite-body-induced potential φ_2

$$\phi(x,y,z) = x + \varepsilon\varphi_1(x,y) + \varepsilon^2\varphi_2(x,r,\theta) + \cdots \tag{26}$$

In the vicinity of the parasite-body axis, the parent-body-induced potential is expanded in Taylor series

$$\frac{\partial\varphi_1}{\partial y}(x, \varepsilon R\cos\theta) = \frac{\partial\varphi_1}{\partial y}(x,0) + \varepsilon\frac{\partial^2\varphi_1}{\partial y^2}(x,0)R\cos\theta + \cdots \tag{27}$$

where $\bar{\alpha}(x) \equiv \frac{\partial\varphi_1}{\partial y}(x,0)$ is the induced angle of attack $\alpha(x) = \varepsilon\bar{\alpha}(x)$. In accord with the slender-body theory, the parasite body is replaced

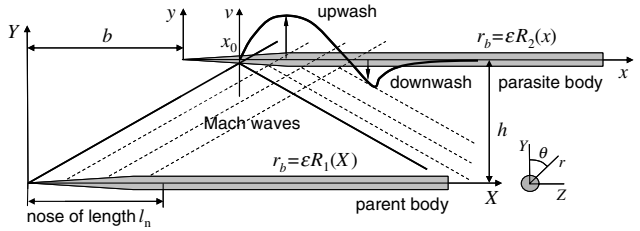

Fig. 12 Interference of two slender bodies in supersonic flow.

by distributions of sources and doublets along the body axis. Then the radial velocity in the body vicinity is approximated as

$$\frac{\partial\varphi_2}{\partial r} \simeq \frac{f(x)}{2\pi r} + \frac{\sigma(x)}{2\pi r^2}\cos\theta, \qquad r \to 0 \tag{28}$$

Calculating the normal velocity v_n on the parasite-body surface and satisfying the boundary condition $v_n = 0$, one can obtain intensities of sources $f(x)$ and doublets $\sigma(x)$. In the leading-order approximation, an asymmetric part of the pressure coefficient, which contributes to the lift, is $C_{P,L} = 2\varepsilon^2 \cos\theta[\bar{\alpha}(x)R_2^2(x)]'$. Integration of $C_{P,L}$ over the body surface gives the axial distribution of lift coefficient

$$C_L(x) \equiv \frac{L^*(x)}{\frac{1}{2}\rho_\infty^* U_\infty^{*2} S_{\max}^*} = 2\int_0^x \alpha(x)A_2'(x)\mathrm{d}x + 4\int_0^x \alpha'(x)A_2(x)\mathrm{d}x$$
$$0 < x < 1 \tag{29}$$

where $x = x^*/l^*$, and $A_2(x) = \pi R_2^{*2}(x)/A_{2,\max}^*$ is the cross-sectional area referenced to its maximum value. The first term in Eq. (29) is associated with the body shape variation $A_2'(x) \neq 0$, whereas the second is related to axial variations of the induced angle of attack $\alpha'(x) \neq 0$. For uniform flow of constant angle of attack $\alpha' = 0$ Eq. (29) specializes to the classic formula of slender-body theory. Note that Eq. (29) agrees with the early results [6,21] derived using an inductive rather than the foregoing deductive asymptotic approach. In contrast to the former, the latter framework provides a foundation of systematic accuracy refinement.

The induced angle of attack $\alpha(x)$ is calculated as follows. The nondimensional potential induced by the parent body is

$$\phi_1(X,Y,Z) \equiv \frac{\phi_1^*}{U_\infty^* l^*} = -\frac{1}{2\pi}\int_0^{X-\beta r} \frac{A_1'(\xi)\mathrm{d}\xi}{\sqrt{(X-\xi)^2 - \beta^2 r^2}}$$
$$r^2 = Y^2 + Z^2 \tag{30}$$

$$A_1(\xi) = \pi R_1^2(\xi), \qquad A_1'(\xi) = 2\pi R_1(\xi)R_1'(\xi) \tag{31}$$

In the symmetry plane $Z = 0$, the induced vertical velocity is expressed as

$$v(Y,X) \equiv \frac{v^*}{U_\infty^*} = \frac{\partial\phi_1}{\partial Y}(X,Y,0) = -\frac{1}{2\pi}\int_0^{X-\beta Y} \frac{\beta^2 Y A_1'(\xi)\mathrm{d}\xi}{[(X-\xi)^2 - \beta^2 Y^2]^{3/2}}$$
$$X > \beta Y \tag{32}$$

On the parasite-body axis $Y = h$ where pv is the principle value

$$v(h,X) = -\frac{1}{2\pi}\,\mathrm{pv}\int_0^{X-\beta h} \frac{\beta^2 h A_1'(\xi)\mathrm{d}\xi}{[(X-\xi)^2 - \beta^2 h^2]^{3/2}}, \quad X > \beta h \tag{33}$$

Accounting for Eq. (31) and using the approximation $\alpha \approx v$, one can get

$$\alpha(h,X) = -\beta^2 h\,\mathrm{pv}\int_0^{X-\beta h} \frac{R_1(\xi)R_1'(\xi)\mathrm{d}\xi}{[(X-\xi)^2 - \beta^2 h^2]^{3/2}}, \qquad X > \beta h \tag{34}$$

Here the principle value of integral is expressed as

$$\mathrm{pv}\int_0^\eta \frac{f(\xi,\eta)}{(\eta-\xi)^{3/2}}\mathrm{d}\xi = I_0(\eta) - \frac{2f(\eta,\eta)}{\sqrt{\eta}} - 2f_\xi'(\eta,\eta)\sqrt{\eta}$$
$$I_0 = \int_0^\eta \frac{f(\xi,\eta) - f(\eta,\eta) - f_\xi'(\eta,\eta)(\xi-\eta)}{(\eta-\xi)^{3/2}}\mathrm{d}\xi \tag{35}$$

where the nonsingular integral I_0 is calculated numerically.

B. Comparison with Euler CFD and Local Solutions

Results of the global analysis were compared with the Euler CFD solutions discussed in Sec. II.D and with the local solution of scattering theory (Sec. II.B). At first consider the case when the parent-body disturbance interacts with the cylindrical part of the parasite body. Because $A_2(x) = 1$ and $A_2'(x) = 0$ in the interaction region, the global solution in Eq. (29) gives $C_L(x) = 4\alpha(x)$, where the induced angle of attack $\alpha(x)$ is calculated using the far-field asymptotic of the slender-body theory solution for the parent body. Figure 13 compares the theoretical distributions of $C_L(x)$ with the numerical data.

The global solution in Eq. (29) can be used for quick evaluation of the lift for different relative distances between the interacting bodies. As an example, Fig. 14 shows the normalized lift coefficient $G_L \equiv C_{L,\text{total}}/\varepsilon^2$ as a function of x_0: the streamwise distance from the parasite-body tip to the point where the parent-body-induced shock crosses the parasite-body axis (Fig. 12). In this case, Eq. (29) is expressed as

$$C_{L,\text{total}}(x_0) = 2\int_{x_0}^l \alpha(x)A_2'(x)\mathrm{d}x + 4\int_{x_0}^l \alpha'(x)A(x)_2\mathrm{d}x$$
$$= 4\alpha(l)A_2(l) - 2\int_{x_0}^l \alpha(x)A_2'(x)\mathrm{d}x \tag{36}$$

For large and positive x_0, when the parent-body-induced shock impinges on the cylindrical part of the parasite body, the total lift is zero in accord with the scattering theory. In the range $-0.3 < x_0 < 1$, the shock interacts with the parasite-body nose and induces a negative lift, that is the parent body attracts the parasite body. As x_0 decreases further, the shock does not cross the parasite-body surface and the lift changes its sign, that is the parent body repels the parasite body. Such a nontrivial behavior of the lift may lead to intricate trajectories of the parasite body during separation.

The theoretical solution in Eq. (15) of the scattering problem allows us to identify governing dimensionless parameters and formulate the scaling law

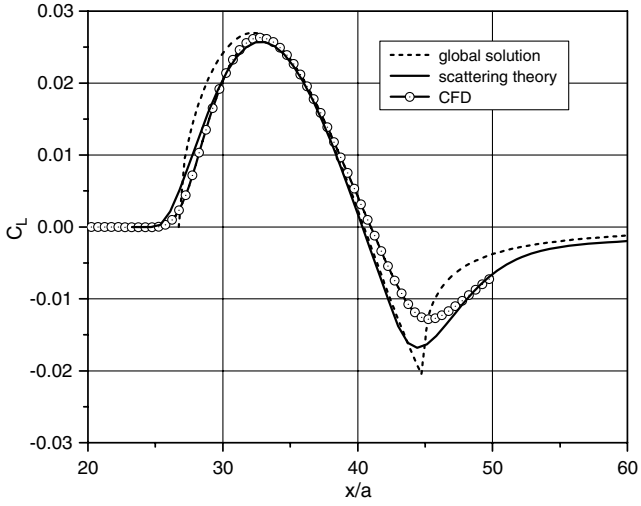

Fig. 13 Comparison of theoretical and CFD distributions of the integral lift coefficient, $M_\infty = 2, h = 16a, l_n = 18a$; interaction occurs on the cylindrical afterbody.

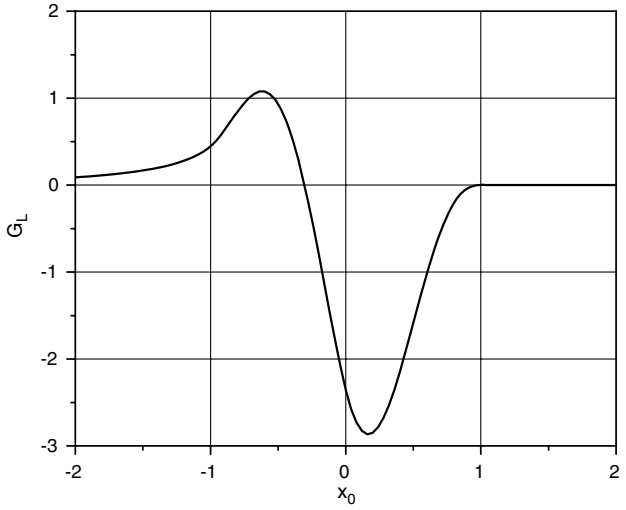

Fig. 14 Normalized lift coefficient $G_L \equiv C_{L,\text{total}}/\varepsilon^2$ as a function of the streamwise relative distance x_0; $M_\infty = 2$; $h = l_n = 1$.

$$C_L = C_{L,\text{ref}} \left(\frac{a}{a_{\text{ref}}}\right)^2 \sqrt{\frac{h_{\text{ref}}\beta}{h\beta_{\text{ref}}}} \tag{37}$$

To illustrate the robustness of this scaling, parametric calculations of the normalized lift coefficient distributions $G_L(x_0) \equiv C_{L,\text{total}}/\varepsilon^2$ were performed at different vertical distances h between two identical bodies (Fig. 15) and different Mach numbers M_∞ (Fig. 16). These dependencies quickly collapse to a universal curve as h and/or M_∞ increases. The discrepancy is less than 10% for $h > 1$ in Fig. 15 and for $M > 2$ in Fig. 16. Thus, the scaling in Eq. (37) can be used for interpolation/extrapolation of CFD solutions and diminishing of the computational effort that is important for quick assessments of aerodynamic coefficients at various time moments during the separation process.

IV. Interaction of a Slender-Body of Revolution with 2-D Wing

The global analysis of Sec. III holds for the case when a slender body of revolution (parasite body) separates from a 2-D wing (parent body). As an example consider the body–wedge configuration schematically shown in Fig. 17. The wedge-induced shock impinges on the body surface and generates the lift. If the shock crosses the cylindrical body part, then the solution Eq. [15] of scattering problem provides distribution of the local lift and predicts the total lift

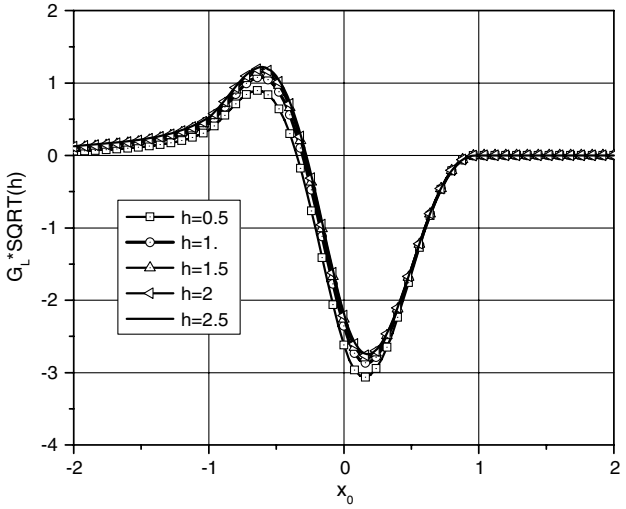

Fig. 15 Normalized lift coefficient distributions $G_L(x_0) \equiv C_{L,\text{total}}/\varepsilon^2$ for different distances h; $M_\infty = 2$; $l_n = 1$.

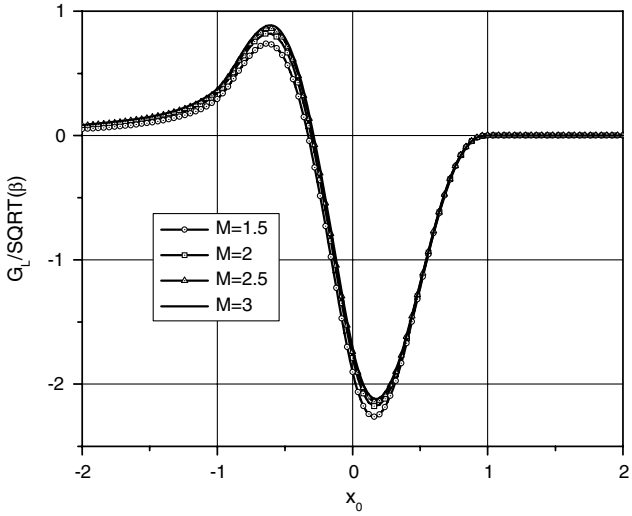

Fig. 16 Normalized lift coefficient distributions $G_L(x_0) \equiv C_{L,\text{total}}/\varepsilon^2$ for different freestream Mach numbers; $h = l_n = 1$.

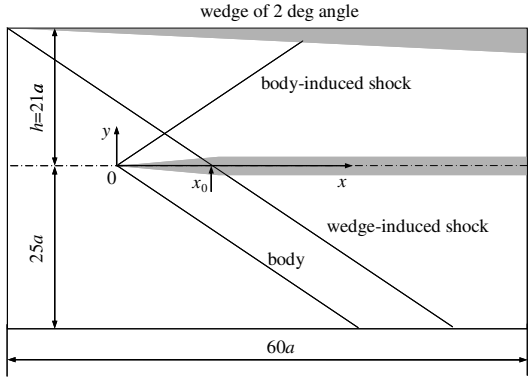

Fig. 17 Computational domain for 3-D Euler simulation of the body–wedge interaction.

$C_{L,\text{total}} = 4\varepsilon$, where ε is the wedge slope. In this case, the global solution in Eq. (29) gives

$$C_L(x) = 4\int_0^x \alpha'(x)A_2(x)\mathrm{d}x = 4\varepsilon H(x - x_0) \tag{38}$$

where x_0 is the streamwise coordinate of the shock-body crossing (Fig. 17) and predicts the same total lift $C_{L,\text{total}} = 4\varepsilon$. Note that the local solution [15] of scattering theory provides the inner structure of shock-body interaction, whereas the global solution ignores these details.

The global solution in Eq. (29) is also applicable to the case when the wedge-induced shock impinges on the body nose having a variable cross-sectional area or passes ahead of the body nose. This allows us to calculate the total lift coefficient at different x_0. Similar calculations were carried out using a 3-D Euler solver for the freestream Mach number $M_\infty = 2$. The computational domain is shown in Fig. 17. A sharp wedge of 2 deg half-angle is located on the upper boundary. The body nose has the length $l_n = 20a$ and radius $r_b = a\sin(\pi x/2l_n)$, $0 \le x \le l_n$. CFD solutions were obtained in a wide range of the wedge-induced shock locus x_0. Figure 18 shows examples of the static pressure field in the symmetry plane for different x_0. The total lift coefficients were calculated using these numerical solutions and compared with the theoretical solution in Eq. (29) and Fig. 19. When the body is completely behind the shock ($x_0 < 0$), the lift is associated with the wedge-induced upwash, and the lift coefficient is given by the classic formula $C_L = 2\alpha$. When the shock crosses the cylindrical afterbody ($x_0 > l_n$, Fig. 18a), the lift is due to the shock scattering, and the lift coefficient is $C_L = 4\alpha$ in accord with Eq. (38). In between ($0 < x_0 < l_n$, Fig. 18b) the shock

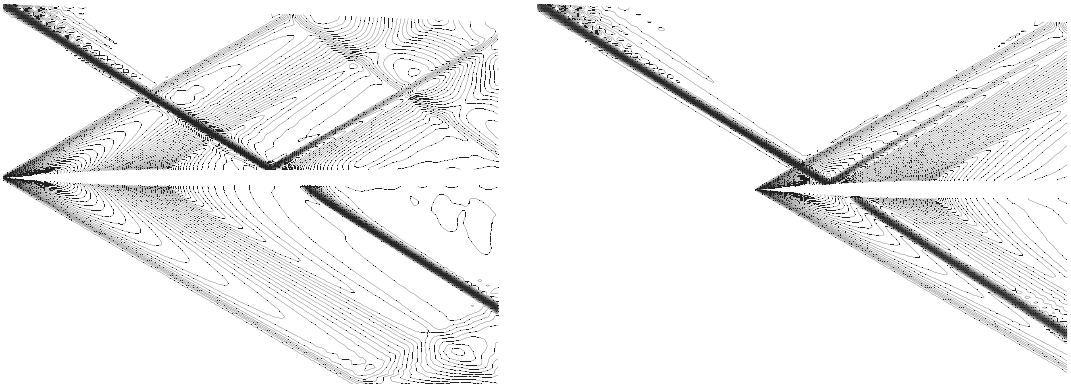

a) b)

Fig. 18 Static pressure contours in the symmetry plane: the body nose is upstream from the wedge-induced shock; a) crosses the wedge-induced shock and b) $M_\infty = 2, l_n = 20a, h = 21a$.

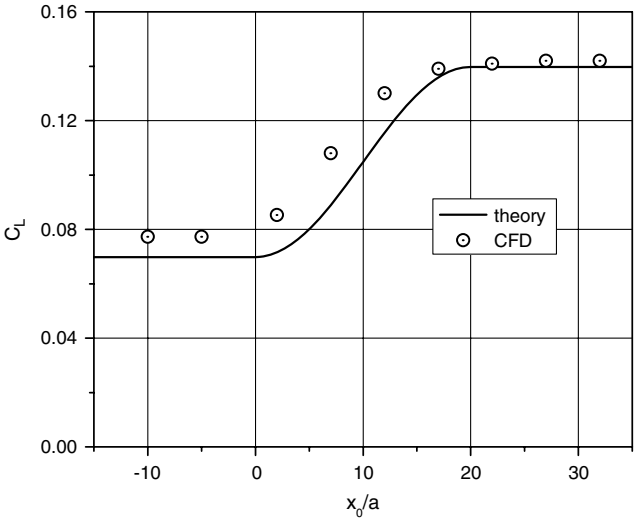

Fig. 19 Total lift coefficient as a function of the normalized shock locus x_0/a, where the black line shows the theoretical solution in Eq. (29), and the symbols show the 3-D Euler solution; $M_\infty = 2, l_n = 20a$.

crosses the body nose, and both mechanisms contribute to the lift. For all cases, the theoretical solution agrees with numerical data within the relative accuracy about 10%. The discrepancy can be reduced by considering the higher-order terms of the asymptotic approximation.

V. Conclusions

The lift due to the interaction between two slender bodies of revolution in a supersonic flow has been analyzed using the linear scattering theory and asymptotic methods. A leading-order asymptotic solution of the scattering problem provides the local and integral lift (acting on the parasite body) in compact analytical forms. These solutions agree satisfactorily with 3-D Euler CFD solutions obtained for two identical bodies in the Mach = 2 freestream. The theory tremendously simplifies predictions of the lift force during the separation process. A combination of these results with the wave-train solutions [14] developed for the wave drag can be used for quick estimates of aerodynamic loads on interacting bodies with very low computational cost.

The lift coefficient was also obtained with the help of global analysis in which the parasite body is replaced by distributions of sources and doublets along the body axis. The analytical expression for the lift coefficient agrees with the early results [21], which were derived using an inductive rather than the discussed herein deductive asymptotic approach. In contrast to the former, the latter provides a foundation of systematic accuracy refinements. Even more important, we showed an analytical connection to the unit scattering problem, which to our knowledge was not previously elucidated. It was demonstrated that the results of global analysis agree with the Euler CFD solutions and with the local solutions of scattering theory. The global solution can be used for quick estimates of the lift for different relative locations of the interacting bodies.

The theoretical analysis provides governing dimensionless parameters and a scaling law. Using this scaling it is feasible to interpolate/extrapolate CFD solutions and diminish the computational cost that is important for quick assessments of aerodynamic coefficients at various instants of the separation process.

The global analysis was also applied to the body-wing configuration. The theoretical lift coefficient agrees with 10% accuracy with the Euler CFD solutions for a slender body having the nose length ~20 body radii.

Acknowledgment

This work was supported by the U.S. Air Force of Scientific Research under contract FA9550-05-C-0030. The views and conclusions herein are those of the authors and should not be interpreted as necessarily representing the official policies or endorsements, either expressed or implied, of the U.S. Air Force Office of Scientific Research or the U.S. government.

References

[1] Goodwin, F. K., Dillenius, M. F. E., and Nielsen, J. N., "Prediction of Six-Degree-of-Freedom Parasite Body Separation Trajectories at Speeds up to the Critical Speed. V.1. Theoretical Methods and Comparison with Experiment," U.S. Air Force Flight Dynamics Lab., Rept. TR-72-83, Oct. 1972.

[2] Wood, M. E., "Application of Experimental Techniques to Store Release Problems," *Proceedings of NEAR Conference on Missile Aerodynamics*, National Technical Information Service, Springfield, VA, 1989, pp. 5.1–5.44.

[3] Nielsen, J. N., *Missile Aerodynamics*, McGraw–Hill, New York, 1960.

[4] Schindel, L. H., "Store Separation," AGARD AG-202, June 1975.

[5] Gapcynski, J. P., and Carlson, H. W., *A Pressure-Distribution Investigation of the Aerodynamic Characteristics of the Body of Revolution in the Vicinity of a Reflection Plane at Mach Numbers 1.41 and 2.01*, NASA Research Memorandum L54129, Jan.–1955.

[6] Gapcynski, J. P., and Carlson, H. W., *The Aerodynamic Characteristics of a Body in the Two-Dimensional Flow Field of a Circular-Arc Wing at a Mach Number 2.01*, NACA Research Memorandum L57E14, July 1957.

[7] Bonnefond, T., Adamov, N. P., Brodetsky, M. D., Vassenev, L. G., Derunov, E. K., and Kharitonov, A. M., "An Experimental Investigation of Aerodynamic Interference of TSTO Winged Systems During Separation. 1. Experimental Technique. Distributed Aerodynamic Characteristics," *Thermophysics and Aeromechanics*, Vol. 3, No. 3, 1996, pp. 213–223.

[8] Bonnefond, T., Adamov, N. P., Brodetsky, M. D., Vassenev, L. G., Derunov, E. K., and Kharitonov, A. M., "An Experimental Investigation

of Aerodynamic Interference of TSTO Winged Systems During Separation. 2. Total Aerodynamic Characteristics of Separated Stages," *Thermophysics and Aeromechanics*, Vol. 34, No. 4, 1996, pp. 285–293.

[9] Belk, D. M., Janus, J. M., and Whitfield, D. L., "Three-Dimensional Unsteady Euler Equations Solution on Dynamic Grids," *AIAA Journal*, Vol. 25, No. 9, 1987, pp. 1160–1161. doi:10.2514/3.9761

[10] Lijewski, L. E., and Suhs, N., "Time-Accurate Computational Fluid Dynamics Approach to Transonic Store Separation Trajectory Prediction," *Journal of Aircraft*, Vol. 31, No. 4, 1994, pp. 886–891. doi:10.2514/3.46575

[11] Thoms, R. D., and Jordan, J. K., "Investigation of Multiple Body Trajectory Prediction Using Time Accurate Computational Fluid Dynamics," AIAA Paper 95-870, June, 1995.

[12] Prewitt, N. C., Belk, D. M., and Maple, R. C. "Multiple-Body Trajectory Calculations Using the Beggar Code," *Journal of Aircraft*, Vol. 36, No. 5, 1999, pp. 802–808. doi:10.2514/2.2513

[13] Malmuth, N., "Theoretical Aerodynamics in Today's Real World: Opportunities and Challenges," *AIAA Journal*, Vol. 44, No. 7, 2006, pp. 1377–1392. doi:10.2514/1.18234

[14] Malmuth, N., and Shalaev, V., "Theoretical Modeling of Slender Bodies Interaction in Supersonic Flows," AIAA 2004-1127, Jan. 2004.

[15] Fedorov, A. V., Malmuth, N. D., and Soudakov, V. G., "Supersonic Scattering of a Wing-Induced Incident Shock by a Slender Body of Revolution," *Journal of Fluid Mechanics*, Vol. 585, Aug. 2007, pp. 305–322. doi:10.1017/S0022112007006714

[16] Landau, L. D., and Lifshits, E. M., *Theoretical Physics, Vol. 6: Hydrodynamics*, Nauka Publishing House, Moscow, 1986 (English translation).

[17] Ashley, H., and Landhal, M., *Aerodynamics of Wings and Bodies*, Addison Wesley Longman, Reading, MA, 1965.

[18] Abramovitz, M., and Stegun, I. A. (ed.), *Handbook of Mathematical Functions with Formulas, Graphs and Mathematical Tables*, Dover, Mineola, NY, June 1964, p. 199.

[19] Roe, P. L., "Characteristic Based Schemes for the Euler Equations," *Annual Review of Fluid Mechanics*, Vol. 18, Jan. 1986, pp. 337–365. doi:10.1146/annurev.fl.18.010186.002005

[20] Chakravarthy, S. R., and Osher, S., "A New Class of High Accuracy TVD Schemes for Hyperbolic Conservation Laws," AIAA Paper 85-0363, 1985.

[21] Moskowitz, B., *Approximate Theory for Calculation of Lift of Bodies, Afterbodies, and Combinations*, NACA TN 2669, April 1952.

Z. Rusak
Guest Editor